ELSEVIER

Physica D 173 (2002) 153–177

PHYSICA D

www.elsevier.com/locate/physd

A manifold independent approach to understanding transport in stochastic dynamical systems

Erik M. Bollt [a,*], Lora Billings [b], Ira B. Schwartz [c]

[a] *Department of Mathematics and Computer Science, Clarkson University, Potsdam, NY 13699-5815, USA*
[b] *Department of Mathematical Sciences, Montclair State University, Upper Montclair, NJ 07043, USA*
[c] *Naval Research Laboratory, Code 6792, Plasma Physics Division, Washington, DC 20375, USA*

Received 3 April 2002; received in revised form 1 August 2002; accepted 2 August 2002
Communicated by E. Ott

Abstract

We develop a new collection of tools aimed at studying stochastically perturbed dynamical systems. Specifically, in the setting of bi-stability, that is a two-attractor system, it has previously been numerically observed that a small noise volume is sufficient to destroy would be zero-noise case barriers in the phase space (pseudo-barriers), thus creating a pre-heteroclinic tangency chaos-like behavior. The stochastic dynamical system has a corresponding Frobenius–Perron operator with a stochastic kernel, which describes how densities of initial conditions move under the noisy map. Thus in studying the action of the Frobenius–Perron operator, we learn about the transport of the map; we have employed a Galerkin–Ulam-like method to project the Frobenius–Perron operator onto a discrete basis set of characteristic functions to highlight this action localized in specified regions of the phase space. Graph theoretic methods allow us to re-order the resulting finite dimensional Markov operator approximation so as to highlight the regions of the original phase space which are particularly active pseudo-barriers of the stochastic dynamics. Our toolbox allows us to find: (1) regions of high activity of transport, (2) flux across pseudo-barriers, and also (3) expected time of escape from pseudo-basins. Some of these quantities are also possible via the manifold dependent stochastic Melnikov method, but Melnikov only applies to a very special class of models for which the unperturbed homoclinic orbit is available. Our methods are unique in that they can essentially be considered as a "black-box" of tools which can be applied to a wide range of stochastic dynamical systems in the absence of a priori knowledge of manifold structures. We use here a model of childhood diseases to showcase our methods. Our tools will allow us to make specific observations of: (1) loss of reducibility between basins with increasing noise, (2) identification in the phase space of active regions of stochastic transport, (3) stochastic flux which essentially completes the heteroclinic tangle.

PACS: 02.50; 05.45; 47.52; 87.23; 05.40; 05.60

Keywords: Stochastic dynamical systems; Stochastic Frobenius–Perron operator; Stochastic transport; Stochastic heteroclinic tangle; Epidemiology; Measles; Noise; Stochastic chaos; Stochastic bifurcation

* Corresponding author.
E-mail address: bolltem@clarkson.edu (E.M. Bollt).
URL: http://www.clarkson.edu/bolltem

0167-2789/02/$ – see front matter
PII: S0167-2789(02)00659-0

1. Introduction

Noise in deterministic dynamical systems plays a prominent role in many cases observed in Nature. For example, noise may induce order in spatio–temporal systems [1], enhance signal to noise ratios in systems modeled by multi-basins of attractions [2], and may even induce phase transitions in wave fronts [3]. These few examples illustrate that noise may indeed be the cause of a global change in real dynamical systems. In the past, this has not been the typical thinking. For example, noise does not have much of an effect on chaotic dynamics. Chaos in deterministic systems has been found to be robust to noise as long as parameters are tuned away from any bifurcation point. This raises the questions of when can noise induce global changes in a system and what are these new emergent dynamics.

Recently, progress has been made in attempting to understand the global role of noise, whereby global we refer to the sampling of phase space containing qualitatively different behavior. For example, in cases where two steady states are separated in phase space and possess distinct basins of attractions, additive noise may cause basin hopping between the two states. Such phenomena have been the focus of the new field of stochastic resonance [2], for which sufficiently large noise causes a communication of sorts between previously isolated basins. The stochastic dynamics is based upon a well-defined probability density function (PDF) describing how much time is spent in each basin. This is primarily a local result. It leads to a statement about exit times from a region, which is important for signal detection, but is not concerned with the dynamics outside the basins.

In contrast to basin hopping, the idea that the dynamics occurring outside the basins may form the basis for understanding many observed fluctuations in Nature. One theoretical approach is based upon the idea of a stochastic Melnikov function, which adds noise to a system possessing deterministic global structure [4]. For many of these systems, analytic details must be known a priori from the deterministic system; i.e., typically, a known homoclinic orbit must exist in the unforced conservative case, so that a perturbation analysis may be completed [5,6]. The advantage is that parameter regions may be computed to find necessary conditions for noise induced chaos and phase space chaotic transport. Similar to other stochastic analysis methods, mean escape times from certain basins may be found, but analysis does not reveal information regarding communication between different regions of phase space [7].

Another example of noise influencing global dynamics occurs in population models of large number of interacting species, such as in population dynamics of epidemics [8] or in the semi-classical modeling of lasers [9]. In contrast to the Melnikovian models, these models do not possess global structure to perturb in the conservative unforced cases. Therefore, all the deterministic and stochastic Melnikov analysis cannot be applied. However, there do exist regions of parameters in which several periodic orbits co-exist, and more importantly, several unstable periodic orbits co-exist. In [10], it was shown that when noise is added to the populations in a simple epidemic model, a sufficient condition for the dynamics to resemble a stochastic version of chaos was the existence of bi-instability. That is, it was found that for parameters generating isolated period two and period three orbits along with two unstable orbits, noise with a small standard deviation could be added to cause trajectories to move outside the basins of the stable attractors. Moreover, it was found that noise caused a sampling of newly created unstable orbits, and when ensemble averaged, gave a positive Lyapunov exponent. This was also seen in models of noise driven lasers [9].

In all the above cases mentioned, a well-defined PDF may be found which describes how phase space is weighted. The disadvantage is that transport of the phase space is missing. Unlike the Melnikov approach, no lobe dynamics are found explicitly viz. the transverse crossing of stable and unstable manifolds. This is especially true if one is working in parameter regions in which there are no transverse manifold intersections; i.e., there may be a pre-tangency condition in which noise will complete a stochastic version of the manifold crossings. Moreover, general stochastic systems do not have well-defined basins of attraction, which is critical in determining transport regions. The main goal of this paper is to develop a theory that will allow one to compute phase space transport without a priori knowledge of the basin boundaries. The basin boundary deficiency in phase space can be overcome

by bringing to bear the tools from dynamical systems coupled with graph theory. Specifically, we will show how to construct a directed graph which details transport from one basin to another when noise is added to a deterministic dynamical system.

Considering a random dynamical system as an independent identically distributed (i.i.d.) composition of deterministic dynamical systems, and thus appropriately weighing a random composition of the corresponding deterministic Ulam transition matrices, has been shown to be a good method to model ergodic properties of stochastic dynamical systems [11]. In particular, this approach has been adapted to model mean and variance of firing times of squid neurons [12]. While some of the techniques via the i.i.d. collection of random dynamical systems method are similar to our methods based on directly projecting the stochastic Frobenius–Perron operator, we would like to highlight regions of high transport activity.

Our approach will be to develop the PDF analysis through the Frobenius–Perron operator, which will allow us to consider any noise distribution, with compact support. We will then use the results to make a finite dimensional projection of the operator onto a set of functions that characterize the mass transport from one phase space region to another. Then, to see how each part of phase space communicates with other parts, we make use of a matrix representation from graph theory. Our approach has the advantage that it may be applied to any reasonably low-dimensional stochastic dynamical system.

The layout of the paper is as follows. In Section 2, we briefly describe a motivating model from population dynamics, which describes the spread of disease in a large population. Since noise induced chaos has been the focus of a large number of papers for this class of models, it is a good one to detail our results. Section 3 describes the details of the Frobenius–Perron operator formalism for computing invariant densities, and its stochastic analogue. In Section 4, a finite dimensional projection of the FP operator is defined, and transport in phase space is defined in terms a Galerkin matrix. Section 5 forms the crux of our paper, which details how transport across boundaries may be automatically computed based on the use of directed graphs. An illustrative one-dimensional example is presented in Section 6, and Section 7 considers the two-dimensional example of the population model. As a natural consequence of the theory, flux across boundaries is immediate, and is presented in Section 8. Expected escape time is derived in Section 9 and conclusions are presented in Section 10. Finally, some remarks about the accuracy of Markov partitions are included in Appendix A.

2. An example of noise-induced chaos

A standard system used to study and predict the stochastic dynamics of disease epidemics is based on the well-known SEIR model [13,14], where the acronym will be clear from the definitions below. We start with a description of the deterministic model and use notation similar to Schwartz and Smith [8]. Assume that the population is sufficiently large so that the various subgroups may be assumed to be continuous. Therefore, the population can be described by four subgroups which evolve in time: Susceptible $S(t)$, those individuals that may contract the disease; Exposed $E(t)$, those individuals that have come in contact with an infectious individual but not yet infectious; Infective $I(t)$, those individuals capable of transmitting the diseases; Recovered $R(t)$, those who are recovered. These groups are disjoint because the recovered enjoy permanent immunity. A child becomes susceptible after losing infant immunity, and then will always fall in one of the four stages. The population can be normalized to $S + E + I + R = 1$, so all dependent variables represent fractions of the population.

A susceptible individual becomes exposed after contact with another infective. This contact rate fluctuates with the seasons and can be approximated in several ways. For ease of exposition, we choose sinusoidal forcing, $\beta(t) = \beta_0(1 + \delta \cos 2\pi t)$, where $0 \leq \delta < 1$. Another more realistic option is term-time forcing, which sets transmission rates high during school terms and low otherwise [15]. However, the form of the seasonal forcing is not critical for our

argument. After a period of latency, the exposed child becomes infective and eventually recovered. Other parameters used to quantify the dynamics are birth rate, μ, the mean latent period, α^{-1}, and the infectious period, γ^{-1}.

Theoretical and numerical analysis show that for almost all cases, the infective and exposed population follow each other in time to first-order [8]. Since the dynamics from the exposed to the infective classes are governed by linear kinetics, it is easy to show that although the SEIR model is three-dimensional, the dynamics collapses onto a two-dimensional surface and the infectives are roughly proportional to the exposed class. The reduction then describes a modified SI model (MSI), given by

$$S'(t) = \mu - \mu S(t) - \beta(t) I(t) S(t), \qquad I'(t) = \left(\frac{\alpha}{\mu + \gamma}\right) \beta(t) I(t) S(t) - (\mu + \alpha) I(t). \tag{1}$$

The standard parameter values for measles are fixed at $\mu = 0.02$, $\alpha = 1/0.0279$, $\gamma = 1/0.01$, $\beta_0 = 1575.0$, and we vary δ, the fluctuating contact rate amplitude [8].

The solutions of the MSI model as well as the bifurcation diagrams for the above set of parameters agree quite well with those of the full SEIR model. For a full description of the deterministic solutions, see [10]. Since the MSI model is periodically driven with period one and both S and I are fractions of the population, it may be a viewed as a two-dimensional map of the unit box into itself. The stochastic model is considered to be discrete as well for the purposes of this paper. That is, noise is added to the population rate equations periodically (period $= 1$) at the same phase having mean zero and standard deviation σ. The dynamics may then be represented as a map, $F : \Re^2 \to \Re^2$,

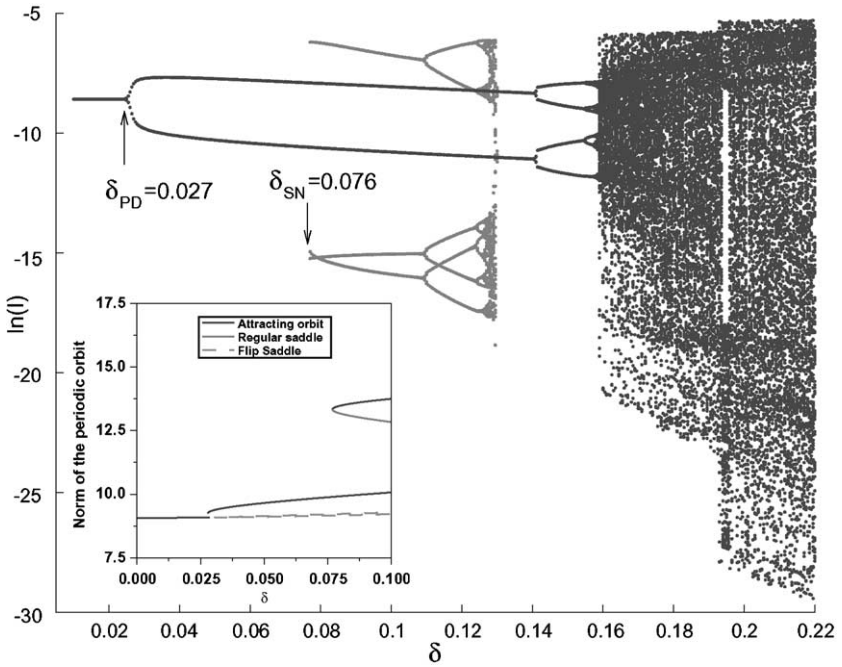

Fig. 1. A bifurcation diagram of the stable periodic and chaotic outbreaks as a function of the contact rate, δ. There are two co-existing attractors. One has a period doubling cascade which leads to naturally occurring chaos for sufficiently large values of δ, and the other branch is created by a period three saddle-node bifurcation. The insert is a bifurcation diagram of the norms, or size, of the stable and unstable periodic outbreaks shown as a function of δ. A stable period one branch undergoes a period doubling bifurcation at $\delta = 0.027$, giving rise to an unstable flip saddle, the dashed line, and a stable period two orbit. The period three cycles appear as a stable–unstable pair at $\delta = 0.076$. The saddle-node bifurcation facilitates bi-instability with the co-existence of two unstable orbits.

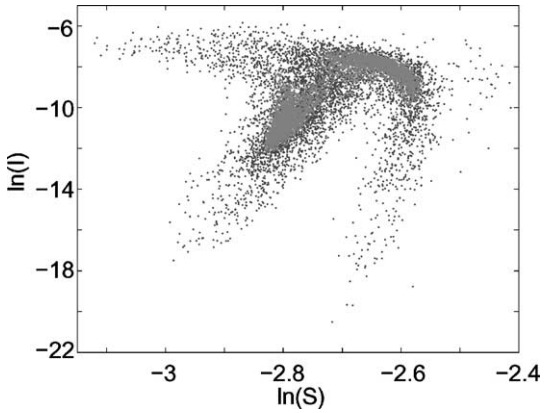

Fig. 2. Stochastic dynamics realizations of MSI model. The computations were done for parameters in the bi-instability region, $\delta = 0.095$. The dense inner trajectory (noisy periodic behavior) has a standard deviation of 0.02, while the sparse outer trajectory (chaotic-like behavior) has a standard deviation of 0.05.

where

$$(S, I)(t+1) = F[(S, I)(t)] + \eta(t).$$

Here $\eta(t)$ is a discrete noise term. To understand the mechanisms for the onset of chaos-like behavior in the presence of noise, we plot two separate bifurcation pictures in the parameter space. In Fig. 1, only attractors are shown as a function of contact rate fluctuations, δ, leading to natural chaos. The insert shows both stable and unstable periodic cycles in the norm, highlighting the unstable branches of the bifurcations. At $\delta = 0.027$, a period doubling bifurcation causes the stable period one to become an unstable annual cycle, or a flip saddle, and creates a stable, period two orbit corresponding to a biennial outbreak. At $\delta = 0.076$, a saddle-node bifurcation creates stable and unstable period three orbits. Without noise, trajectories starting in the neighborhood of the stable period two or period three orbits simply converge to one of these two attractors. The unstable periodic points only play a small part in lying on the basin boundaries, which are not fractal. Notice when the period three attractor appears, there exists a period two attractor, as well as unstable period one and period three orbits (saddles). Since the mechanism for inducing chaos with noise is determined by the interaction of the two unstable cycles, we define this region in parameter space as a *region of bi-instability*. In [10] it was shown that the existence of bi-instability is a sufficient condition for noise to excite chaos. That is, there exists a sufficiently large standard deviation in which new unstable orbits are created and sampled. It was also demonstrated that in the deterministic case, only periodic orbits exist, and no underlying topological horseshoe is formed. When sufficient noise is added, it completes a partially formed heteroclinic tangle, thus forming an unstable stochastic version of a topological horseshoe. An example of how noise changes the dynamics globally in the region of bi-instability is presented in Fig. 2.

3. Density evolution and the Frobenius–Perron operator

First, we define the Frobenius–Perron operator for a deterministic function. Associated with a discrete dynamical system acting on initial conditions, $\mathbf{z} \in M$ (say, $M \subset \Re^n$)

$$F : M \to M, \qquad x \mapsto F(x) \tag{2}$$

is another dynamical system over $L^1(M)$, the space of densities of ensembles of initial conditions

$$P_F : L^1(M) \to L^1(M), \qquad \rho(x) \mapsto P_F[\rho(x)]. \tag{3}$$

This Frobenius–Perron operator (P_F) is defined by the continuity equation [16]

$$\int_{F^{-1}(B)} \rho(x)\,dx = \int_B P_F[\rho(x)]\,dx \tag{4}$$

for measurable sets $B \subset M$. Differentiation changes this operator equation to the commonly used form[1]

$$P_F[\rho(x)] = \int_M \delta(x - F(y))\rho(y)\,dy \tag{5}$$

acting on probability density functions $\rho \in L^1(M)$.

Next, we lay out the basic idea for computing a PDF when the dynamics are known. Both deterministic and stochastic cases are considered for dynamics that are discrete. Now we consider the stochastically perturbed dynamical system

$$F_\nu : M \to M, \qquad x \mapsto F(x) + \eta, \tag{6}$$

where η is a random variable with PDF $\nu(x)$, which is applied once each iteration. The random part ν is assumed to be independent of state x which we tacitly assume to be relatively small, so that the deterministic part F has primary influence.

The "stochastic Frobenius–Perron operator" has a similar form to the deterministic case [16]

$$P_{F_\nu}[\rho(x)] = \int_M \nu(x - F(y))\rho(y)\,dy, \tag{7}$$

where the deterministic kernel, the delta function in Eq. (5), now becomes a stochastic kernel describing the PDF of the noise perturbation.

In this paper, we will assume for specificity that the external noise is normal

$$\nu(x) = \frac{1}{\sqrt{2\pi\sigma^2}} \exp\left(-\frac{\|x\|^2}{2\sigma^2}\right) \tag{8}$$

with mean $x = 0$ and standard deviation σ as the adjustable parameter. Therefore, Eq. (7) becomes

$$P_{F_\sigma}[\rho(x)] = \frac{1}{\sqrt{2\pi\sigma^2}} \int_M e^{-\|(x-F(y))\|^2/2\sigma^2} \rho(y)\,dy. \tag{9}$$

We write "P_{F_σ}" to emphasize the normal distribution involved. This form of the noise is justified for the particular application system we study, roughly by invoking the usual central limit theorem argument due to many added outside noise influences. Most of our analysis does not rely on this specific form of the noise, and carries through similarly if some other noise term is justified.

4. Approximation of the infinite dimensional operator

We use the Galerkin method to approximate the Frobenius–Perron operator by a Markov operator of finite rank. This method is most commonly found in nonlinear pde's to resolve differential operators [17]. We use a projection

[1] The other common form of the Frobenius–Perron operator being, $P_F[\rho(x)] = \sum_{y:y=F^{-1}(x)} \rho(y)/|F'(y)|$, where the sum is taken over all pre-images of F.

of the infinite dimensional linear space $L^1(M)$, with discretely indexed basis functions $\{\phi_i(x)\}_{i=1}^{\infty} \subset L^1(M)$ onto a finite dimensional linear subspace generated by a subset of the basis functions [18], $\Delta_N = \mathrm{span}(\{\phi_i(x)\}_{i=1}^{N})$, such that $\phi_i \in L^1(M)\ \forall i$. This projection, $p : L^1(M) \to \Delta_N$ is realized optimally by the Galerkin method in terms of the inner product, which we choose to be integration, $(f, g) \equiv \int_M f(x)g(x)\,\mathrm{d}x, \forall f, g \in L^2(M)$. Specifically, the infinite-dimensional "matrix" becomes the $N \times N$ matrix

$$A_{i,j} = (P_{\mathrm{F}_\sigma}[\phi_i], \phi_j) = \int_M P_{\mathrm{F}_\sigma}[\phi_i(x)]\phi_j(x)\,\mathrm{d}x, \quad 1 \le i, j \le N. \tag{10}$$

One approximate $\rho(x)$, by the finite sum of basis functions is

$$\rho(x) \simeq \sum_{i=1}^{N} d_i \phi_i(x). \tag{11}$$

We discuss the quality of this approximation in Appendix A.

The historically famous Ulam's method [19], devised for a one-dimensional map setting, formulates matrix entries as

$$A_{i,j} = \frac{m(B_i \cap f^{-1}(B_j))}{m(B_i)} \tag{12}$$

with the interpretation of the fraction of B_i which maps to B_j. (Here, $m(\cdot)$ denotes the Lebesgue measure on M.) This Ulam matrix, which approximates the deterministic Frobenius–Perron operator equation (5) is easily shown to be equivalent to the Galerkin matrix by using Eq. (10) and choosing the basis functions to be the family of characteristic functions

$$\phi_i(x) = \chi_{B_i}(x) = \begin{cases} 1 & x \in B_i, \\ 0 & \text{else.} \end{cases} \tag{13}$$

Specifically, we choose the ordered set of basis functions to be in terms of a nested refinement of boxes $\{B_i\}$ covering M. Though Eqs. (10) and (12) are formally equivalent in the deterministic case, we find that the Galerkin form is more natural in the stochastic setting pursued in this paper. More will be said about how to efficiently compute the large number of matrix elements of $A_{i,j}$, each of which requires a double integral. We develop several numerical analytic techniques to do this efficiently.

In principle there is wide latitude in choice of basis functions, such as the Fourier basis of sines and cosines. The techniques we develop in this paper aim to highlight locations of phase space particularly responsible for mass transport. Hence, the choice of characteristic functions make the phase space locations corresponding to relative density transport, as in Eq. (12), particularly natural, as opposed to some other basis such as the Fourier modes, which would be appropriate instead to highlight evolution of other harmonics.

5. Mass transport and stochastic matrices

The matrix approximation of the Frobenius–Perron operator, $A_{i,j}$ is a Markov operator of finite rank, and as such, it can be interpreted as a transition matrix: $A_{i,j} > 0$ implies that there is a mass of initial conditions, amongst an ensemble of initial conditions, that moves from box B_i to box B_j upon one application of the stochastic dynamical system, Eq. (6). For a typical noise distribution, such as normal

$$\nu(x) = \frac{1}{\sqrt{2\pi\sigma^2}} \exp\left(-\frac{\|x\|^2}{2\sigma^2}\right),$$

which has nonzero support everywhere, there is everywhere a positive probability of mass transport. However, we are concerned with significant probability, above some tail threshold. See Section 5.2 for more discussion of numerically computing $A_{i,j}$, which includes masking negligible values. In Section 5.3, we describe how the matrix can be re-indexed to conveniently lay plain the transport regions of the original stochastic dynamical system.

5.1. Review of some graph theory—irreducible matrices

First we review some language from graph theory [20,21] to describe the action of the transition matrix A. Let, G_A be the directed graph generated by a matrix A. G_A consist of edges E and vertices V

$$G_A = (E, V), \tag{14}$$

where the set of vertices, $V = \{v_i\}_{i=1}^N$ label the original boxes $\{B_i\}_{i=1}^N$, and the edges are defined to be the set of ordered pairs of integers $E = \{(i, j) : i, j \in 1, \ldots, N, A_{i,j} > 0\}$ which label the vertices as their starting and ending points. Given any two vertices v_i and v_j, there exists a *minimal path distance* denoted $\mathrm{dist}(v_i, v_j)$, which is the number of vertices in a shortest path through the unweighted graph, allowing that $\mathrm{dist}(v_i, v_j) \equiv \infty$ if v_i is not path connected to v_j.[2] A graph is defined to be *reducible* if there exists a vertex v_i and a vertex v_j such that there exists no path through the graph between them. Otherwise, it is *irreducible*. Said in terms of the transition matrix A, G_A is irreducible iff there exists an $m > 0$ such that $A^m_{i,j} > 0\ \forall(i, j)$. The diameter of a graph is defined as the longest minimal path in the graph, $\mathrm{diam}(G_A) = \max_{i,j} \mathrm{dist}(v_i, v_j)$. Let us form the matrix $C = \sum_{n=1}^N A^n$. Since the diameter of a finite graph, which is not infinite, is bounded by the number of vertices, $\mathrm{diam}(G_A) \leq N$, it follows that G_A is irreducible iff $C_{i,j} > 0\ \forall(i, j)$, and $C_{i,j} = 0 \Rightarrow$ there exists no path from v_i to v_j. Note that the discrete term "irreducible" corresponds roughly to the term "ergodic" in dynamical systems, and the equivalence can be made exact for a Markov map.

Now we assume that G_A has a reducible subcomponent. Suppose there is a decomposition $V = V_1 \cup V_2$, such that V_1 communicates with V_1 and V_2, but V_2 communicates only with V_2. That is, a re-indexing of the vertices transforms A into a block matrix of the form

$$R = \begin{pmatrix} R_{1,1} & R_{1,2} \\ \mathbf{0} & R_{2,2} \end{pmatrix}, \tag{15}$$

where $R_{1,1}$ and $R_{2,2}$ have the same number of rows and columns as vertices in V_1 and V_2, respectively. Eq. (15) is the canonical form of a reducible matrix. However, for our specific application in which R is a re-ordered Galerkin matrix derived from a bi-stable dynamical system, it is common to find the special block dynamical matrix form in which $R_{1,2} = \mathbf{0}$; such is called "completely reducible", or "decomposable" [22]. By definition, exchanging/relabeling the index naming vertices v_i and v_j, $i \leftrightarrow j$, of a graph corresponds to exchanging rows and columns i and j of A, for which there exists an appropriate permutation matrix. Since a permutation is a similarity transformation, $R = P^{-1}AP$, or linear conjugacy, all dynamically relevant invariants are preserved. Therefore, completely re-indexing a graph can be achieved by pair exchanges, by a sequence of such permutations. Roughly in terms of dynamical systems language, the vertices V_1 are the stable invariant set, and while V_2 may have an unstable invariant set (cycling-paths in the graph), it includes the basin of V_1. Note that it is often the case that the transition matrix $R_{1,1}$, of the reduced subcomponent V_1, may itself have a further subdecomposition into the same form as Eq. (15).

If it is known that A is similar to a matrix R written in the canonical form of Eq. (15), the problem is to decide which vertices to re-index $V_1 = \{v_{k_1}, v_{k_2}, \ldots, v_{k_m}\}$ as those which are path connected to all. Then, the rest shall

[2] The "Breadth First Search" algorithm may be used to compute $\mathrm{dist}(v_i, v_j)$, [20,21].

be $V_2 = \{v_{k_{m+1}}, v_{k_{m+2}}, \ldots, v_{k_N}\}$. One may identify these two sets of vertices by application of the Breadth First Search algorithm, which signals those vertices v_i such that some v_j have $\mathrm{dist}(v_i, v_j) = \infty$. In the next section, we discuss a direct method to identify appropriate re-indexing, by consideration of the underlying dynamical system.

In the native boxes $\{B_i\}$ covering M, there is a natural spatial indexing, say for example a "raster" scanning of the grid covering M. However, the graph representation of the resulting graph G_A has no special dimensional information from M, or spatial orientation. This is an advantage in that the techniques we develop below intelligently re-index the box covering set $\{B_i\}$, and therefore the corresponding vertex set V, to achieve the form equation (15), will work equally well for a wide range of dynamical systems of various dimension and attractor characteristics essentially as a black-box tool.

5.2. Near sparse Galerkin matrices and link-lists

Consider storage size and access time to the Galerkin matrix A. If there is an attractor in a compact region of the phase space, then we cover with a grid of $N \equiv m^n$ rectangles $\{B_i\}_{i=0}^N$, resulting in an $N \times N$ matrix $A_{N\times N}$. For example, even our modest MSI model has $n = 2$, and choosing $m = 100$ results in $N = 10^4$ which requires a $N \times N = 10^4 \times 10^4$ matrix. This brute-force approach of storage scales rapidly as m^{2n}. Furthermore, each matrix element $A_{i,j}$ requires an accurate numerical evaluation of the n^2-dimensional integral in Eq. (10), which requires its own fine grid to control that error. The key short cut is to notice the near sparse nature of A.

5.2.1. Negligible matrix entries and negligible integration

Here we discuss numerical issues which greatly reduce the computation time necessary to compute the matrix A, approximating the stochastic kernel. Inspection of the Frobenius–Perron operator, Eq. (9), reveals that most matrix entries are negligible in computer machine precision. Likewise those matrix entries, which are not negligible, may theoretically communicate with all other matrix entries due to normal noise, but such communication quickly drops below the machine precision threshold. Substituting the definition of the Frobenius–Perron operator P_{F_σ}, Eq. (9), into the definition of a matrix element, $A_{i,j} = (P_{\mathrm{F}_\sigma}[\phi_i], \phi_j)$ in Eq. (10), and using the choice of characteristic basis functions from Eq. (13), reduces the range of the double n-dimensional integrals considerably

$$A_{i,j} = \frac{1}{\sqrt{2\pi\sigma^2}} \int_M \int_M \mathrm{e}^{-\|x-F(y)\|^2/2\sigma^2} \chi_{B_i}(y)\chi_{B_j}(x)\,\mathrm{d}y\,\mathrm{d}x = \frac{1}{\sqrt{2\pi\sigma^2}} \int_{B_j} \int_{B_i} \mathrm{e}^{-\|x-F(y)\|^2/2\sigma^2}\,\mathrm{d}y\,\mathrm{d}x. \quad (16)$$

This integrand is usually small and easily bounded. Choose ϵ to be some negligible threshold (say $\epsilon = 10^{-15}$ in double precision arithmetic). Then

$$\frac{1}{\sqrt{2\pi\sigma^2}} \int_{B_j} \int_{B_i} \mathrm{e}^{-\|x-F(y)\|^2/2\sigma^2}\,\mathrm{d}y\,\mathrm{d}x < \frac{1}{\sqrt{2\pi\sigma^2}} \int_{B_j} \int_{B_i} \delta\,\mathrm{d}y\,\mathrm{d}x = \frac{\delta}{\sqrt{2\pi\sigma^2}} m(B_i)m(B_j), \quad (17)$$

if

$$\|x - F(y)\| > \sigma\sqrt{-2\,\ln\,\delta} \quad (18)$$

and we choose

$$\delta = \frac{\epsilon\sqrt{2\pi\sigma^2}}{m(B_i)m(B_j)}, \quad (19)$$

where $m(\cdot)$ denotes Lebesgue measure of a rectangle. That is, if all the points in the ith rectangle, $y \in B_i$, map far away under F from all the points in the jth rectangle, $x \in B_j$, then the matrix entry $A_{i,j}$ should be neglected.

To guarantee inequality (19), we set

$$A_{i,j} \mapsto 0, \quad \text{if } \inf_{x\in B_j, y\in B_i} \|x - F(y)\| > -\sigma\sqrt{2}\,\ln\frac{\delta}{2}. \tag{20}$$

In practice, we consider it safe to replace the infimum with a minimum over several sample points from each rectangle when the boxes are relatively small and assuming that F is continuous. Notice that such considerations can be made a priori entering any multiple algorithmic loops. Without assignment (20), A will always be full, but most entries are exceedingly small, which is what we refer to as "almost sparse".

For example, invoking assignment (20) for the MSI model when $m = 100$ reduces what would be 100×100 grid, and thus the necessary job of computing the $10^4 \times 10^4$ matrix entries of A, for just $Q = 62528$ nontrivial entries when choosing $\epsilon = 10^{-20}$, and $\sigma = 0.001$. For those matrix entries which are not neglected by assignment (20), the integrand is smooth, thus facilitating straightforward application of a wide variety of standard techniques [23] such as Simpson's method to evaluate each $A_{i,j}$ to comparable ϵ accuracy.

5.2.2. Link lists

We now address what would be a formidable storage issue of the matrix A. If A is full, then it is necessary to save all $N \times N = m^{2n}$ entries of the matrix. This tends to be such a large number, even for our relatively modest $m \times m = 100 \times 100$ grid of rectangles covering the MSI attractor, that storage becomes an issue, as does the time necessary to manipulate the full array for the operation of re-indexing. Following the previous section, we showed how A can be well approximated by a highly sparse matrix. In fact, we never form the transition matrix since that would require storing mostly zeros. Instead, we use a link-list representation of the directed graph. A link list L consists of a $Q \times 3$ array including the matrix entry, and two pointers, where Q denotes the number of nonzero entries. Specifically, for each $A_{i,j} > 0$, index a value $k \in 1, \ldots, Q$, and record $L_k = [A_{i,j}, i, j]$. Notice that such a record of the transition matrix A is closely related to the definition of the underlying directed graph in Eq. (14), where an edge is defined as an ordered pair of vertex names. This link list definition is sufficient for all steps of our process, from creating the matrix A in link list format, to re-indexing, to interpretation of the transport back in the native coordinates of the phase space. The storage savings are substantial. If A is full, then $Q = N^2$, and hence L is a larger array with $3N^2$ entries, but if $Q < N^2/3$, then memory is saved, and our matrices are considerably more sparse, as in the MSI example at the end of the last subsection where $Q = 62528$ for $\epsilon = 10^{-20}$, $\sigma = 0.001$, and $N^2 = 10^8$. Roughly, the expectation is that Q will scale as the box counting dimension of the attractor, while N scales as the dimension of the embedding manifold.

5.3. How to re-index

Next, we introduce a method to conveniently re-index the vertices of G_A, the directed graph representation of the action of Frobenius–Perron operator. By "convenient", we wish the matrix representation to lay plain in the regions of transport which leak measure between neighboring basins, across what were transport barriers in the absence of noise. We have in mind the situation in which there is a form of "pre-tangency" stochastic chaos; neighboring basins of stable attraction leak enough measure to overcome the deterministic action of those basins. The problem with a grid approximation of the phase space is that a typical (say raster scanned) ordering of the phase space will tend to have those regions that should be dynamically grouped (those in the same basin) scattered seemingly haphazardly in the indexing. Thus, there is a need for re-indexing.

Our algorithm is designed for the case that we have a deterministic dynamical system, with several stable basins, called a "multistable" system, in which there is a mixing of states as noise amplitude increases. Our algorithm in brief is to:

- Identify vertices corresponding to each basin of attraction in the zero-noise case.
- Re-index the corresponding matrix representation $k_1, k_2, \ldots, k_N$ by row/column exchange elementary permutation operations. Further re-index each vertex according to the number of steps to center of the corresponding basin.
- Gradually turn-up the noise amplitude while maintaining that zero-noise determined vertex order, which was previously computed and dynamically coherent.
- Identify vertices from which measure leaks, and find their position in the original phase space.

It is straightforward to identify vertices v_i whose paths all lead to some attracting vertex v_j (roughly corresponding approximately to $v_i \in \approx \text{basin}(v_j)$). Furthermore, we can identify the number of steps in the path from v_i to v_j. We will sort $\text{basin}(v_j)$ accordingly, to put the stable fixed points of the dynamical system at the heart of each matrix block.

6. A one-dimensional example

We clarify the problem and our solution in terms of the following one-dimensional piecewise linear map, $f : [0, 1] \to [0, 1]$

$$f(x) = \begin{cases} -0.9x + 0.09 & \text{if } x < 0.1, \\ 2.5x - 0.25 & \text{if } 0.1 \le x < 0.5, \\ -2.5x + 2.25 & \text{if } 0.5 \le x < 0.9, \\ -0.9x + 1.81 & \text{if } 0.9 \le x, \end{cases} \tag{21}$$

illustrated in Fig. 3. There are two stable fixed points, $x = 9/19$ and $18.1/19$, with trapping regions $[0, 0.1]$ and $[0.9, 1]$, respectively. There are also two unstable fixed points, $x = 1/6$ and $9/14$. In gray, we show the pre-images of those trapping regions, which are not already in the trapping regions. With zero noise, the picture is simple. Almost every initial condition eventually lands in one of the two trapping regions. This is a one-dimensional bi-stable system. The structure of each basin is shown in Fig. 4. Note that in this example, we know that each of the two basins forms a Cantor set in $[0, 1]$, with a naturally finer and finer scale associated with each successive pre-image of the trapping region.

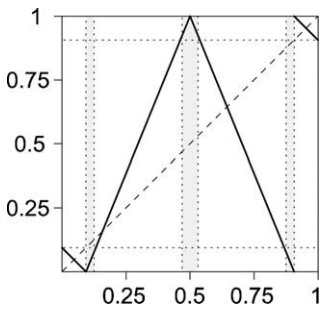

Fig. 3. The one-dimensional map in Eq. (21). The gray overlay indicates the first pre-images of the connected basins of the fixed points.

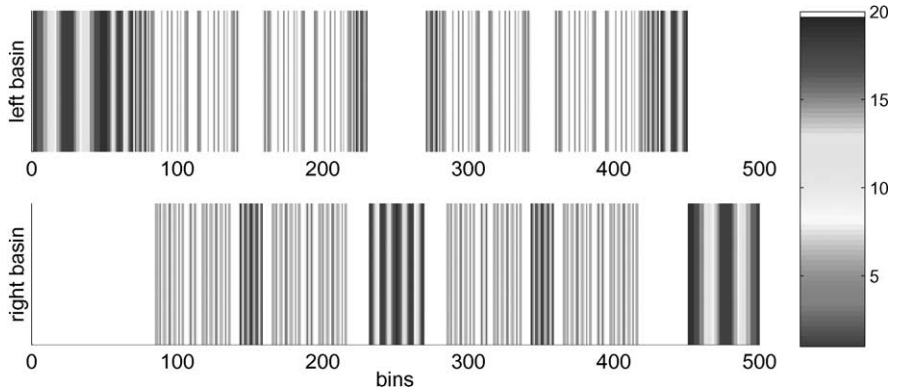

Fig. 4. The basins of the one-dimensional map in Eq. (21) with no noise. The shades of gray represent the number of iterates a bin is away from the fixed point (see the side color bar). The top graph represents the basin of the left fixed point, and the bottom graph represents basin for the right. White represents bins that are not part of that basin. 500 bins were used in this computation.

We choose to order the bins in each basin by their convergence rate to a fixed point. In other words, the ordering depends on the number of iterates the midpoint of the bin is away from the fixed point bin, as shown in Fig. 4. To separate the basins, we put the first basin in ascending order, and the second basin in descending order. Therefore, the fixed points are at the ends and closest to their immediate pre-images. Fig. 5 first shows the natural ordering of the bins, and in the lower graph, shows the re-ordering.

With a small amount of noise added to each iteration of the map in Eq. (21), some initial conditions rarely leave the noiseless trapping regions, due to random perturbations across the gray gaps adjacent to those trapping regions. Such escape becomes more and more likely as the added noise amplitude is increased. This picture is reflected in the family of PDFs depicted in Fig. 6, which we calculated by repeated direct application of the stochastic FP operator, where the integral is calculated numerically, and iteration of an initial uniform distribution is performed to satisfactory convergence. The problem with direct inspection of the stable invariant PDF is that it contains no information about what regions of phase space act as the transport barriers, which are increasingly crossed by the noisy version of the dynamical system. In this simple example, we know that the gray regions in Fig. 3 serve that role, and we will now show that this information can be recovered by an algorithmic black box, given purely an approximation of the Frobenius–Perron operator which reveals the one-step action of the dynamical system on densities.

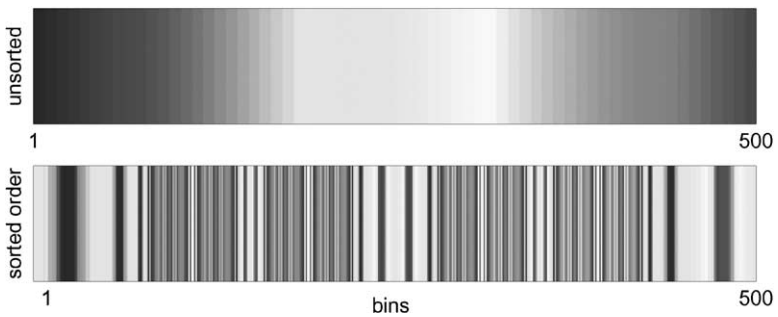

Fig. 5. The re-ordering of the bins in the Galerkin matrix according to basin and the number of iterates a bin is away from the fixed point. The shades of gray in the top graph represents the original unsorted order of the 500 bins. The coloring of the bottom graph shows the sorted re-ordering of the bins.

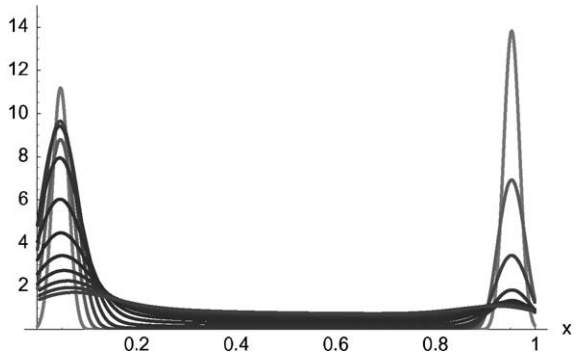

Fig. 6. The one-dimensional map in Eq. (21). Family of PDFs due to increasing normal noise, $\sigma = 0.01$ (curve with largest peaks at the ends of the interval) to $\sigma = 0.12$ (smallest peaks).

In the left graph of Fig. 7, we see the unsorted Galerkin matrix. In the right graph of Fig. 7, we can see the blurring effect of the noise on the Galerkin transfer matrix, which causes noise-induced diffusion of mass across boxes.

In Fig. 8, we see the re-indexed Galerkin matrices for $\sigma = 0.001$ and $\sigma = 0.04$. The thick black lines crossing the middle of the matrix denote the basin boundaries of the graph, and approximate the basin boundaries of the dynamical system. It is these boundaries that the noise-induced transport must overcome, and this feature can now become obvious in this arrangement. At this point, we remark that no structures smaller than the box covering scale can possibly be revealed. The boxes of a scale significantly smaller than the noise perturbations which interest us are not particularly useful, since noise is well known to blur fine scale structures of invariant measure [24]. As indicated by the Galerkin matrix for $\sigma = 0.04$, Fig. 9 marks the intervals, which are five or less iterations away from the interval containing the fixed point, that transport mass to the other basin (in the original phase space).

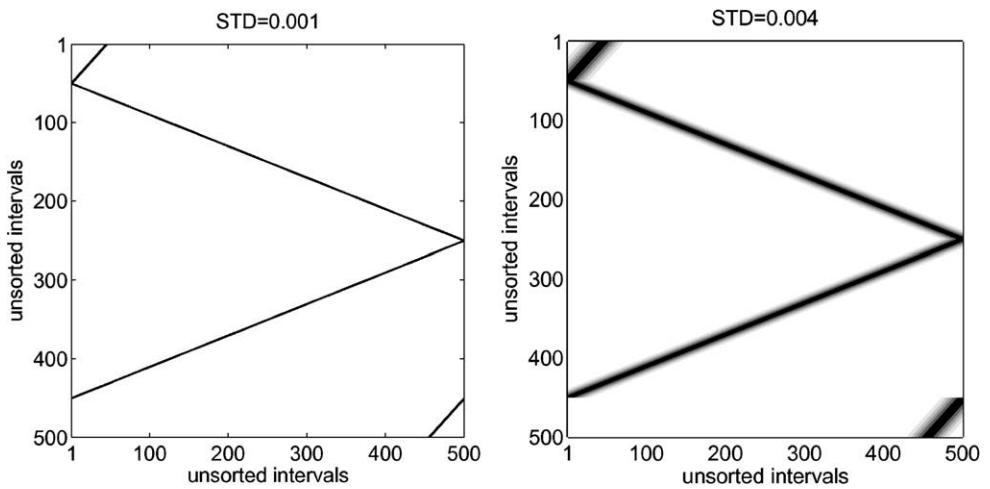

Fig. 7. Galerkin matrix for $\sigma = 0.001$ (left), before re-indexing as in Fig. 8. Note that in the original indexing, this matrix appears as the map in Eq. (21), whose action on densities it represents. With larger noise, $\sigma = 0.04$ (right) we can see the blurring action of the Galerkin transfer matrix. Note that the largest values in the Galerkin matrix are represented by the darkest shades, while white represents values below a threshold considered equivalent to 0.

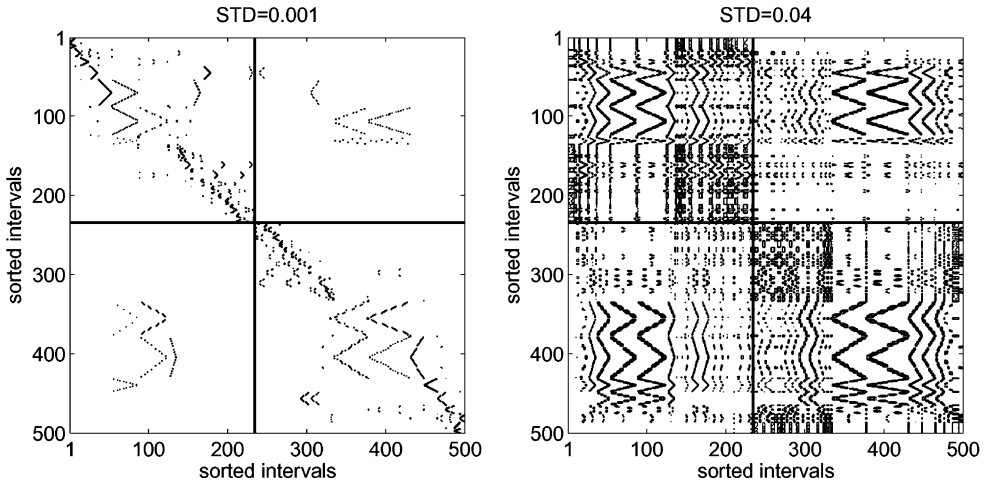

Fig. 8. A representation of the Galerkin matrices for $\sigma = 0.001$ (left) and $\sigma = 0.04$ (right), re-indexed according to the number of iterations away from a stable point. The bold lines separate the two basins. The black indicates where in the matrix values are above a threshold equivalent to 0.

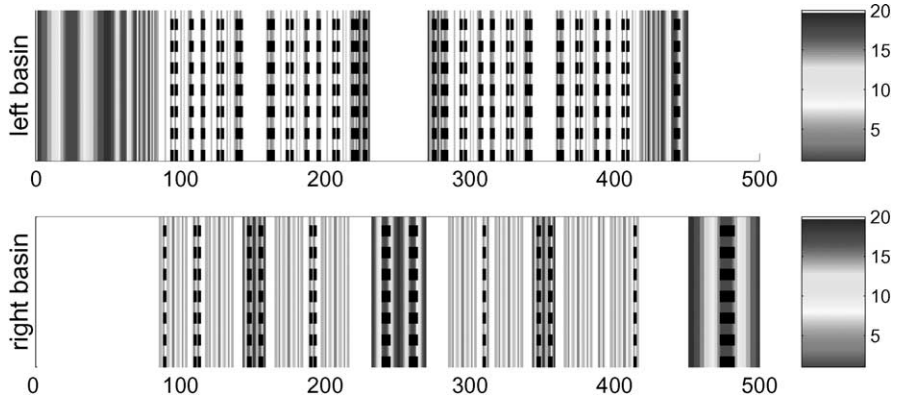

Fig. 9. The escape regions found for $\sigma = 0.04$ labeled by dashed black lines, overlaid on the basin maps for each basin. Only intervals that are five or less iterations away from the interval containing the fixed point are considered.

7. A two-dimensional example

Now we are in the position to study the mechanism behind the noise-induced transport of the MSI model, Eq. (1). In this section, first we apply our newly developed tool to the MSI model, essentially as a black box, to reveal the transport mechanism. Then we interpret the results in terms of what is already known about this dynamical system.

Following the algorithm outlined in Section 5.3 requires little special consideration for our specific system. Once we raster-scan an index to cover the attractor by a coarse grid, the resulting Galerkin matrix approximation of the Frobenius–Perron operator is essentially dimension independent, with no memory of the phase space from which it was formed. A few special considerations are computationally necessary to manage the large-scale of the problem in a $n > 1$-dimensional phase space, such as the $n = 2$ MSI example. These were outlined in Section 5.2.

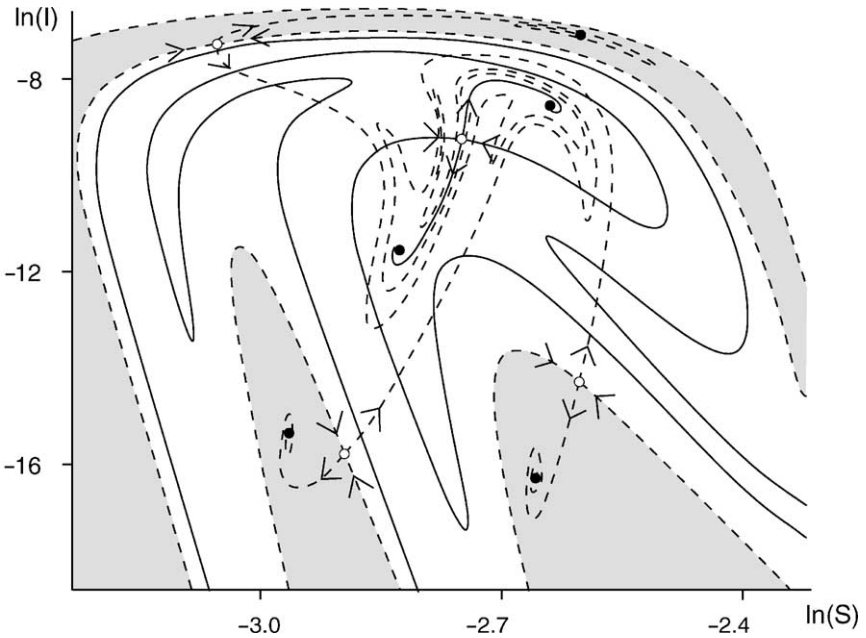

Fig. 10. A graph of the manifolds for the MSI model with $\delta = 0.095$. Stable periodic orbits are in black. The basin of the period two orbit is white and the basin of the period three orbit is gray. The manifolds of the unstable period one orbit are solid black and the manifolds of the unstable period three orbit are dashed. Note the forward-heteroclinic crossings where the solid and dashed manifolds intersect.

We now formulate noise-parameterized discrete models of the Frobenius–Perron operators, corresponding invariant densities, and the main result of our new method, the location of regions and degrees of transport from the re-ordered matrices transformed back to the native phase space. We start by showing the main features of the phase space in Fig. 10. The basins and manifolds of the periodic orbits are shown here. Note the position of the stable period two and period three orbits in phase space. After we split up this part of phase space into 100^2 bins, the bins need to be ordered into two sets, first by basin, and then by number of iterates it is away from the attracting orbit.

In Fig. 11, we see the invariant density of the MSI model, as a function of σ-noise amplitude. These pictures are calculated as the dominant eigenvector of the corresponding Galerkin matrix, which we have remarked is (almost) a stochastic matrix. The essential feature is that when $\sigma = 0$, the two main density spikes are at the dynamic centers of each respective basin. The striking features of interest to us of increasing σ are:

- Initially, the density becomes less diffusely distributed around the stable fixed points, due to predominantly stochastic diffusion on top of the primary dynamic effect, which is the existence of two stable fixed points and two distinct basins.
- A crossover effect occurs, for $\sigma > 0.2$, after which the density mass becomes mixed throughout a larger region, and predominantly mixed between the originally separate basins. This mixing is a larger effect than can be explained by stochastic diffusion. In [10], it was noted that there is initially, $\sigma = 0$, a backward heteroclinic connection, but no forward connection, but the forward connection becomes effectively realized for large enough σ. Thus the argument is that for large enough σ, there is "stochastic chaos".

In this paper, we have formulated a new tool to complement the explanation given in [10]. We directly study the approximated density transport and transport regions.

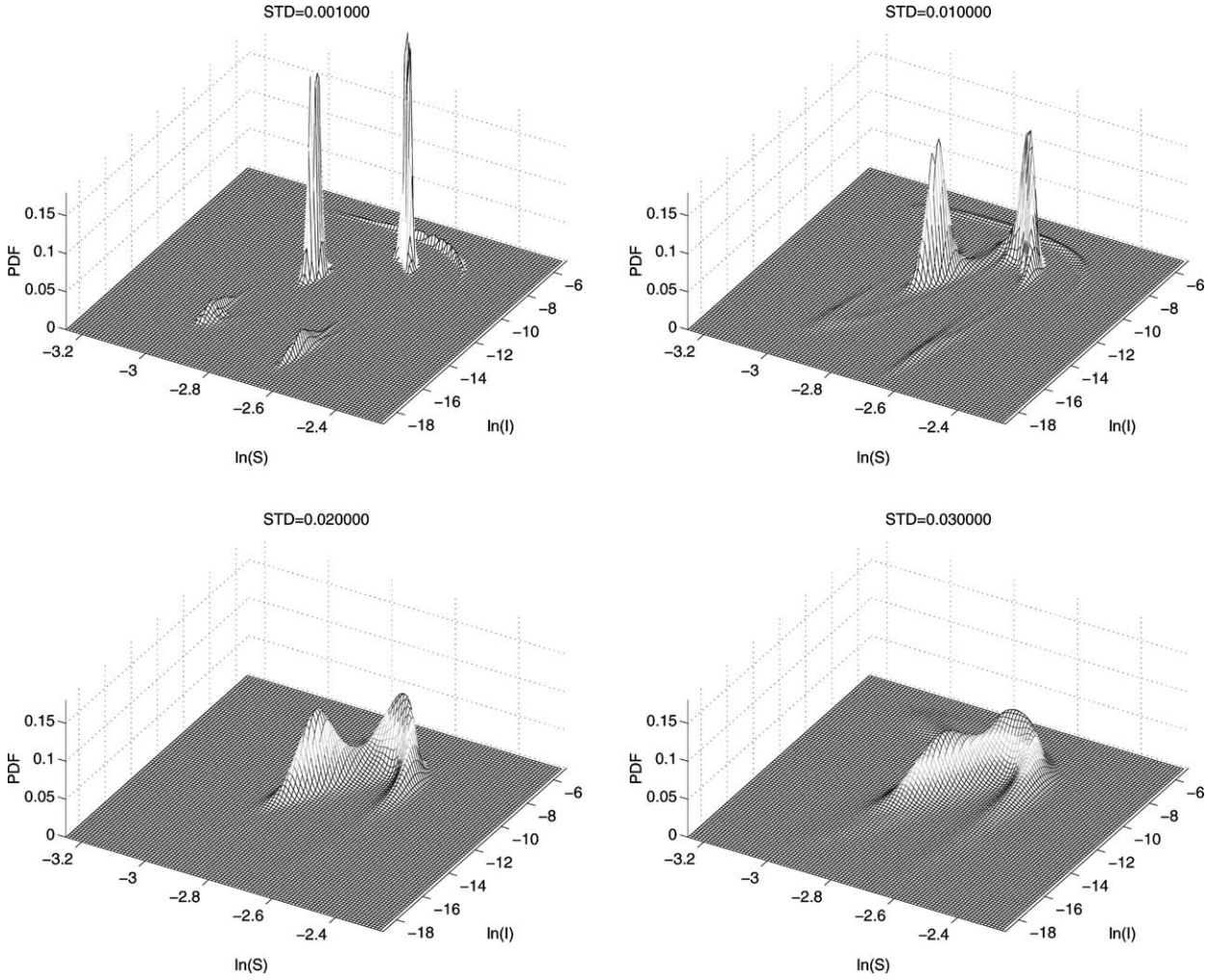

Fig. 11. The PDF as a function of the standard deviation of the noise for the MSI model: $\sigma = 0.001, 0.01, 0.02, 0.03$. The PDF was calculated as the dominant eigenvector of the Galerkin matrix. In the top left graph, the period two orbit is located in the two largest peaks, while the period three is in the three smaller peaks.

Figs. 12 and 13, respectively, bring out two important points of this paper: (1) loss of reducibility between the basins with increasing noise and (2) identification in the phase space of active regions of stochastic transport. In Fig. 12, we see the sorted matrix in the canonical form of Eq. (15). We note that the two off-diagonal submatrices are completely empty when $\sigma = 0$. Maintaining this re-indexing, we see clearly the cause of the density which leaks between the formerly separate basins, which is the loss of reducibility of the corresponding (here approximated) operator; in this sense, understanding Fig. 12 can be considered as one of the main points of this paper. A second main point is that we can recover the location of the most active regions and barriers to stochastic transport, which are now obvious in the re-indexed matrix form shown in Fig. 12. In Fig. 13, we color the two basins by the number of iterates a bin is away from the stable periodic orbit. We overlaid in black stars the bins that send mass to the other basin, facilitating stochastic transport. We only consider bins within five iterates of the stable attractors. Therefore, it is possible for a trajectory that has converged to an orbit to escape to the other basin.

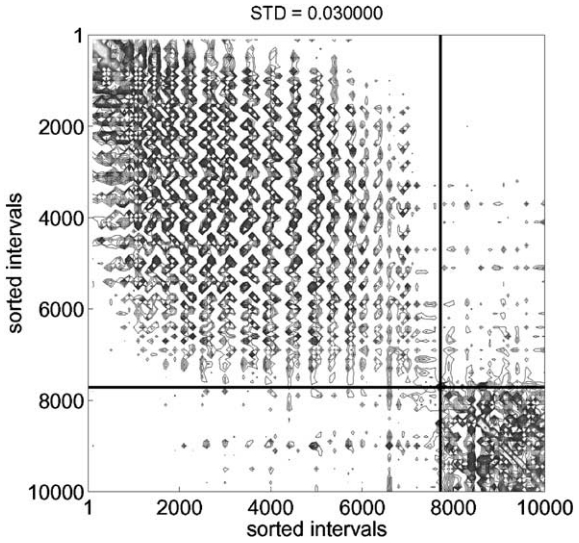

Fig. 12. The sorted Galerkin matrix for the standard deviation $\sigma = 0.03$. The black lines separate the bins of the period two basin from the period three basin.

8. Flux across barriers

When investigating transport, flux across barriers is the natural quantity to calculate. In the above, we have used re-indexing to delineate the zero-noise barriers between basins, which become partial barriers as $\sigma \uparrow$. Given a region, say an open set S, it is possible to define *mass flux* (or simply *flux*) in and out of the region, across the boundary ∂S [25]. In our MSI model, we take S_i, $i = 1, 2$ to be the two basins for $\sigma = 0$. Let,

$$\mathcal{F}_S^{\pm}[\rho] \equiv \text{mass entering/exiting } S \text{ from outside/inside } S \text{ upon one application of the map, due to initial density profile } \rho, \tag{22}$$

where $\mathcal{F}_S^{\pm}[\rho]$ can be read, "mass flux into/out-of S due to an initial density profile ρ". To calculate $\mathcal{F}_S^{+}[\rho]$, we appropriately restrict the region of integration of the stochastic Frobenius–Perron operator, Eq. (9),

$$\mathcal{F}_S^{+}[\rho] = \frac{1}{\sqrt{2\pi\sigma^2}} \int_S \int_{\tilde{S}} \mathrm{e}^{-\|(x-F(y))\|^2/2\sigma^2} \rho(y)\,\mathrm{d}y\,\mathrm{d}x. \tag{23}$$

Here, $\tilde{S}$ denotes the complement of the set S. Observe that the inner integral,

$$\frac{1}{\sqrt{2\pi\sigma^2}} \int_{\tilde{S}} \mathrm{e}^{-\|(x-F(y))\|^2/2\sigma^2} \rho(y)\,\mathrm{d}y$$

gives the density at x which comes from a point $y \in \tilde{S}$, meaning not in S. The outer integral accounts for the total mass of all such contributions in x. To calculate the flux into S, $\mathcal{F}_S^{-}[\rho]$, we must simply reverse the regions of integration in Eq. (23). We state the obvious identities

$$\mathcal{F}_S^{+}[\rho] = \mathcal{F}_{\tilde{S}}^{-}[\rho] \quad \text{and} \quad \mathcal{F}_S^{-}[\rho] = \mathcal{F}_{\tilde{S}}^{+}[\rho] \tag{24}$$

due to conservation of mass. Note that unlike the deterministic case, stochastic transport is drawn from a broad region, due to the diffusive stochastic kernel; this property is indicated clearly by the out-of-decomposed bands seen in Fig. 12.

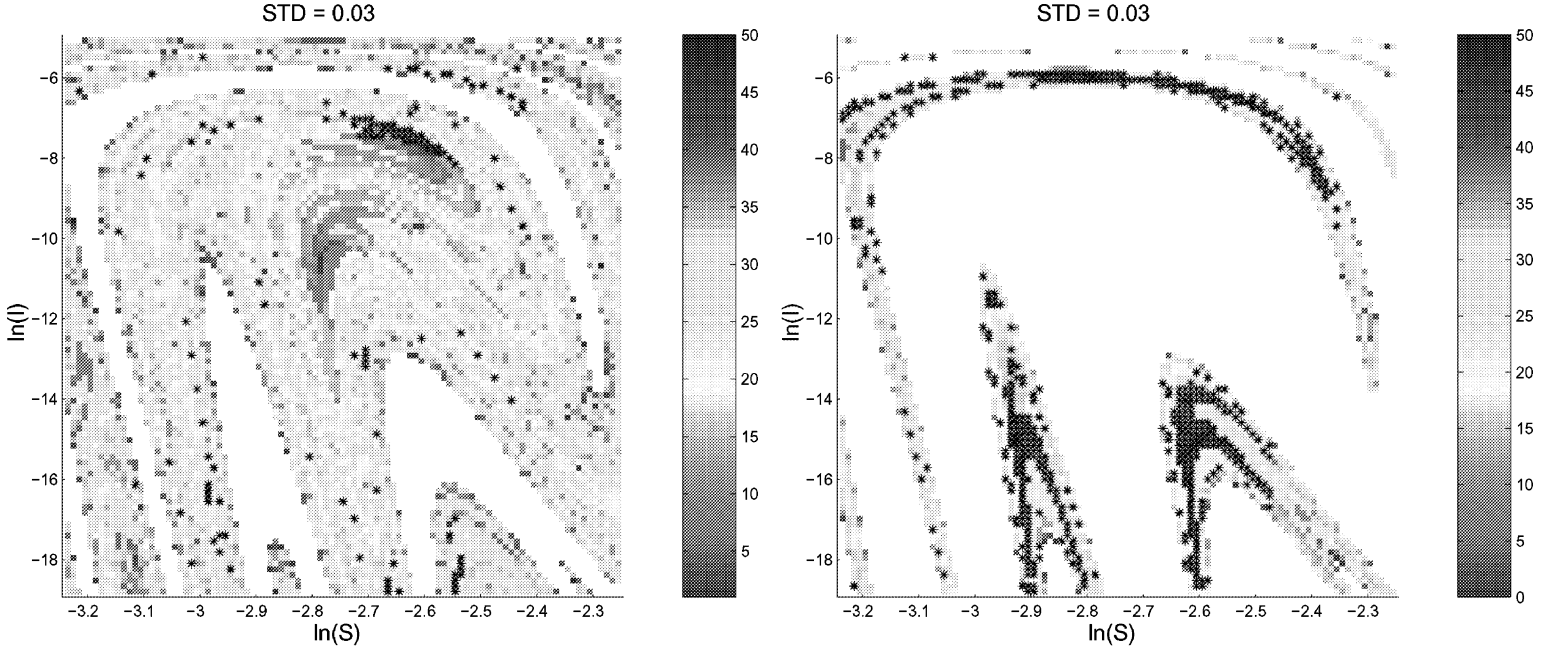

Fig. 13. Escape regions (black stars) for the period two basin (left) and period three basin (right) calculated from Fig. 12 overlaid on the basin of attraction. The color bar indicates the number of iterations from the periodic orbit. The standard deviation is $\sigma = 0.03$. Only bins within five iterations were considered for transport.

One has the option to calculate $\mathcal{F}_S^{\pm}[\rho]$ by direct (numerical) application of Eq. (23). We choose to continue to follow the approximation method on a fine grid, by substitution of Eq. (11), which we justify in Appendix A. The inner integral becomes

$$\frac{1}{\sqrt{2\pi\sigma^2}}\int_{\tilde{S}} \mathrm{e}^{-\|(x-F(y))\|^2/2\sigma^2}\rho(y)\,\mathrm{d}y \simeq \frac{1}{\sqrt{2\pi\sigma^2}}\int_{\tilde{S}} \mathrm{e}^{-\|(x-F(y))\|^2/2\sigma^2}\sum_{i=1}^{N} c_i\chi_{B_i}(y)\,\mathrm{d}y$$
$$= \sum_{i:B_i\cap\tilde{S}\neq\emptyset} c_i \frac{1}{\sqrt{2\pi\sigma^2}}\int_{B_i} \mathrm{e}^{-\|(x-F(y))\|^2/2\sigma^2}\,\mathrm{d}y. \tag{25}$$

Substitution into Eq. (23) gives the approximation

$$\mathcal{F}_S^{+}[\rho] \simeq \sum_{i:B_i\cap\tilde{S}\neq\emptyset} c_i \frac{1}{\sqrt{2\pi\sigma^2}}\int_S\int_{B_i} \mathrm{e}^{-\|(x-F(y))\|^2/2\sigma^2}\,\mathrm{d}y\,\mathrm{d}x$$
$$\simeq \sum_{i:B_i\cap\tilde{S}\neq\emptyset} c_i \int_{\cap_{j:B_j\subset S}B_j}\int_{B_i} \frac{1}{\sqrt{2\pi\sigma^2}} \mathrm{e}^{-\|(x-F(y))\|^2/2\sigma^2}\,\mathrm{d}y\,\mathrm{d}x. \tag{26}$$

We recognize this last double integral, from Eq. (16), to consists of a sum over those entries of matrix $A_{i,j}$ such that $B_i \in \tilde{S}$, and $B_j \in S$. Hence, we define the flux matrix

$$\mathcal{A}_S^{+} \equiv \begin{cases} A_{i,j} & \text{if } B_i \in S \text{ and } B_j \in \tilde{S}, \\ 0 & \text{otherwise,} \end{cases} \tag{27}$$

which allows us to rewrite Eq. (26)

$$\mathcal{F}_S^{+}[\rho] \simeq \|\mathcal{A}_S^{+}\cdot\mathbf{c}\|_1, \tag{28}$$

where $\|\cdot\|_1$ denotes the absolute sum. In this form, we have flux in terms of $\mathcal{A}_S^{+}$, which is a masked transfer matrix, times the coefficient weights vector $\mathbf{c} = (c_1, c_2, \ldots, c_N)^t$. One can similarly form and interpret masked transfer matrices $\mathcal{A}_S^{-}$, $\mathcal{A}_{\tilde{S}}^{+}$ and $\mathcal{A}_{\tilde{S}}^{-}$.

Choosing an initially uniform density $\mathbf{c} = (1/N)\mathbf{1}$, we can find stochastic "area flux". In this case, Eq. (28) reduces to the absolute sum of matrix entries

$$\mathcal{F}_S^{+}[\mathbf{1}] = \sum_{i,j}[\mathcal{A}_S^{+}]_{i,j}. \tag{29}$$

In Fig. 14, we see how both the area flux (left) and PDF flux (right) change as noise volume is increased. We use the term "PDF flux" for the choice ρ is the invariant density substituted into Eq. (28). It is no surprise that area flux increases monotonically as $\sigma \uparrow$. We explain the less intuitive nonmonotonicity of the PDF flux as follows: apparently from $\sigma \simeq 0.01$ to $\sigma \simeq 0.02$, there is a crossover in that while area flux continues to increase, the concentration of density in the region S decreases, and so weighting according to the PDF results in a decreasing PDF flux.

Our flux computations now bring us to another main point of this paper. Stochastic flux essentially completes the heteroclinic connection. Our hypothesis in [10] was that noise completes a partially formed heteroclinic tangle for the MSI model. See Fig. 10 for a graph with the location of the periodic orbits and corresponding manifolds. In Fig. 15, we show the flux with PDF weighting. Again, the PDF flux reveals the combination of the density with the transport, showing where a trajectory is most likely to escape to another basin. Observe in the left graph that the greatest flux occurs where the unstable manifold of the period-one saddle is closest to the stable manifold of the period-three saddle, thus completing the heteroclinic tangle.

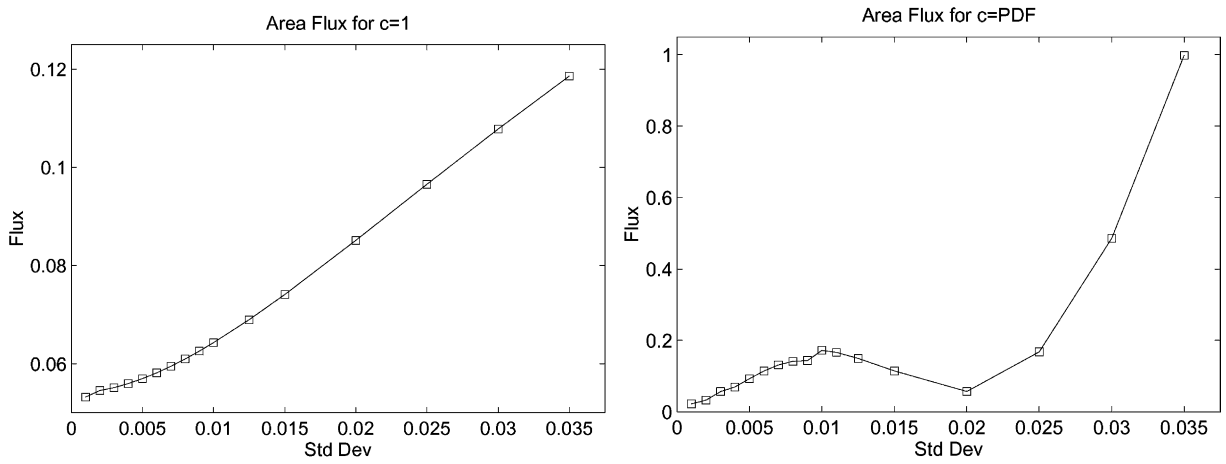

Fig. 14. The flux as a function of the standard deviation (σ). The left diagram is the "area flux", Eq. (29), in terms of a uniform initial density, and the right diagram is "PDF flux" weighted according to the PDF.

9. Expected escape time

Another natural quantity to consider when investigating transport is expected escape time across a barrier of a point in a region. Again, suppose a region S. Given a point $x \in B_i \subset S$, let $T(x)_i$ be the actual time of escape for a particular sample path of the stochastic dynamical system of a randomly chosen initial condition in the ith box. The expected time of escape from S, for a point $x \in B_i \subset S$ is

$$\langle T(x)_i \rangle = \sum_{n=1}^{\infty} nP(T(x) = n) = \sum_{i=1}^{\infty} nP(F^n(x) \notin S \quad \text{and} \quad F^m(x) \in S,\ \forall m < n). \tag{30}$$

The key issue to acknowledge is that we are interested in the mean time of *first* escape. While,

$$A^n_{i,j} = P(F^n(x) \in B_j | x \in B_i), \tag{31}$$

this probability does not forbid multiple passages or recurrences. In particular, it accounts for orbits which might leave S and return to S multiple times before finally landing in $B_j \subset \tilde{S}$ on the nth iterate.

We define an operator which measures the probability of first escape from S, again by restricting (masking) the Galerkin matrix A. Let this "escape matrix" be defined as,[3]

$$[\mathcal{E}_S^-]_{i,j} \equiv \begin{cases} A_{i,j} & \text{if } B_i \in S, \\ 0 & \text{otherwise.} \end{cases} \tag{32}$$

Since $\mathcal{E}_S^-$ has zero probability of a transition of the type, $\tilde{S} \to S$, we now have

$$[\mathcal{E}_S^-]^n_{i,j} = P(F^n(x) \in B_j \subset S \quad \text{and} \quad F^m(x) \in S,\ \ \forall m < n | x \in B_i \subset S) \tag{33}$$

which is exactly the probability of first exit transition that we require to calculate the mean in Eq. (30).

[3] This is an approximation similar to that in Eq. (9), except we have less severely restricted the region of integration of the Frobenius–Perron operator: $(1/\sqrt{2\pi\sigma^2}) \int_S \int_M \mathrm{e}^{-\|(x-F(y))\|^2/2\sigma^2} \rho(y)\, \mathrm{d}y\, \mathrm{d}x$.

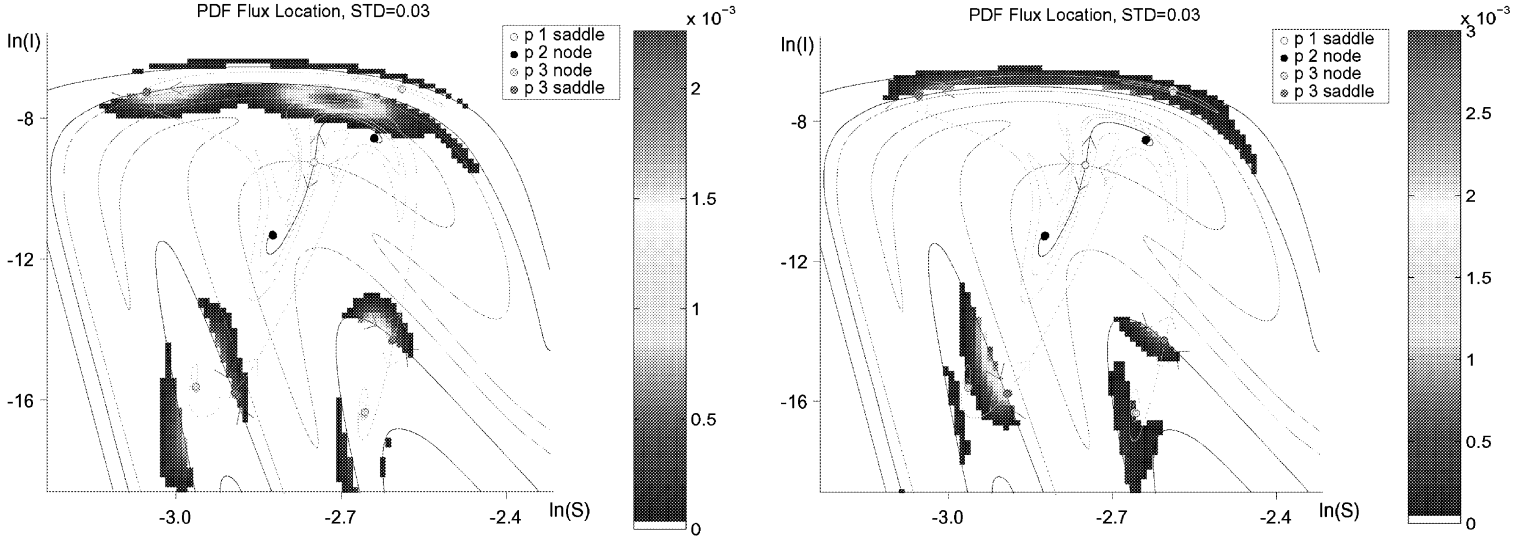

Fig. 15. The PDF flux over the phase space for the period two basin (left) and period three basin (right). The periodic orbits are indicated by the large shaded dots similar to Fig. 10. These graphs show the regions where trajectories escape to other basins. Shades indicate relative rates.

Since the events described in the probability in Eq. (33) are disjoint events for two different target boxes

$$P(F^n(x) \in \cup_{j:B_j\subset\tilde{S}} B_j \quad \text{and} \quad F^m(x) \in S,\ \ \forall m < n | x \in B_i \subset S) = \sum_{j:B_j\subset\tilde{S}} [\mathcal{E}_S^-]_{i,j}^n. \tag{34}$$

We now have the notation necessary to state the following theorem:

Theorem. *If the escape matrix defined in* Eq. (32) *is bounded,*[4] $\|[\mathcal{E}_S^-]\| < 1$, *then the expected mean time of escape from S for an orbit starting in box $B_i \subset S$ to any box $B_j \subset \tilde{S}$ is*

$$\langle \mathcal{T}(B_i) \rangle = \frac{1}{\#\{j : B_j \subset \tilde{S}\}} \sum_{j:B_j\subset\tilde{S}} [[\mathcal{E}_S^-] \cdot (I - [\mathcal{E}_S^-])^{-1} \cdot (I - [\mathcal{E}_S^-])^{-1}]_{i,j}, \tag{35}$$

where $\#\{j : B_j \subset \tilde{S}\}$ is the number of boxes $B_j \subset \tilde{S}$, and $\mathcal{T}(B_i)$ is the time of first escape of a single randomly sampled path starting at B_i, based on paths defined by the graph G_A model of the Frobenius–Perron operator, using Eqs. (10) and (13).

Proof. By Eq. (33)

$$\langle \text{Time of first escape from } B_i \subset S \text{ to } B_j \subset \tilde{S} \rangle = \sum_{n=1}^{\infty} n[\mathcal{E}_S^-]_{i,j}^n. \tag{36}$$

By the assumed bound, $\|[\mathcal{E}_S^-]\| < 1$, we have the matrix geometric series [27]

$$(I - [\mathcal{E}_S^-])^{-1} = \sum_{n=0}^{\infty} [\mathcal{E}_S^-]^n \tag{37}$$

from which it is straightforward to derive

$$\sum_{n=1}^{\infty} n[\mathcal{E}_S^-]^n = [\mathcal{E}_S^-] \cdot (I - [\mathcal{E}_S^-])^{-1} \cdot (I - [\mathcal{E}_S^-])^{-1}. \tag{38}$$

Hence, selecting the ith, jth entry of this matrix on the right side of Eq. (38) gives the mean escape time from S, starting at box B_i, and arriving after n-iterates at box B_j. By independence of the events of arriving at two different boxes B_j and $B_{j'}$, both in $\tilde{S}$, the total mean escape time from box B_i to any box $B_j \subset \tilde{S}$ is the arithmetic mean of the mean escapes times to each individual box, which gives the formula equation (35).

The restriction that $\|[\mathcal{E}_S^-]\| < 1$ is not severe, since in all but a trivial choices of S (when $\|[\mathcal{E}_S^-]\| = 1$, because the matrix A is stochastic), the inequality should hold. □

Now we critique our result. Note that $j : B_j \subset \tilde{S}$ is generally a proper set inclusion due to the imperfect course grid, but Eq. (34) will be approximately the correct probability needed in Eq. (30) for a fine grid. The only part missed is including probability of transitions near the boundary of $\tilde{S}$. By this critique, one expects that $\langle \mathcal{T}(B_i) \rangle \leq \langle T(x)_i \rangle$, but $\langle \mathcal{T}(B_i) \rangle \simeq \langle T(x)_i \rangle$ for a fine grid. However, notice that formula equation (35) gives expectation in terms of the combinatorial model of the Frobenius–Perron operator, formed using a fine grid, and not the full operator. We expect the calculation to be good for a fine grid.

[4] The notation $\|\cdot\|$ used in this section denotes the matrix natural norm, $\|A\| = \sup_{\|u\|=1} \|A \cdot u\|$, in terms of a vector norm, which we could choose here to be the sup-norm, in which case, $\|A\|_\infty = \max_i \sum_j |A_{i,j}|$, [26], which is the maximum column sum.

10. Conclusion

Random dynamical systems, deterministic systems which are considered in the presence of noise, have been growing ever more important in the description of dynamics far from equilibrium. In this paper, we have shown how to compute the invariant density of random dynamical systems necessary to evaluate phase space transport. The main advantage of the techniques we present in Sections 5 and 8 is that transport is computed in the absence of any knowledge of the presence of intersecting manifolds. This is in contrast to the lobe dynamics presented in [5].

The tools used to develop a manifold independent model of transport revolved around computing a finite dimensional analog of the Frobenius–Perron operator, which was defined as a Galerkin matrix. The payoff in using such a representation is that one can map an arbitrary phase space dimension (finite) into a two-dimensional model. Since each element is a measure of the probability of one component of phase space mapping into another, it is now possible to see explicitly how transport between basins occurs as a function of noise strength. This is accomplished with the aid of graph theory, which allows one to re-order the matrix entries in a way in which basin boundaries are easily seen as well as which portions of phase space communicate with each other.

The models we consider, a one-dimensional map and a modified SEIR model (MSI) from epidemiology, form two basic purposes. First, the one-dimensional map is shown in detail to form a tutorial in implementing the theory. It is a bi-stable map, but the basin boundary separating the fixed points is fractal. This poses a problem when considering a re-ordering of the Galerkin matrix, but is circumvented by only considering a finite number of pre-images of the basins that contain the fixed points.

The MSI model is an example of a system that exhibits bi-instability, which has been conjectured to play a role in noise induced chaos in population dynamics [10]. In [10], it was conjectured that the mechanism for stochastic chaos arises from a sufficient amount of noise completing a heteroclinic connection between transverse crossings between stable and unstable manifolds. However, no explicit metric of mixing could be constructed until the development of the tools in this paper. Although the definition of stochastic chaos has not been well-defined, such a computation of transport between different basins can be viewed as a measure of noise induced mixing. That is, in the absence of noise, the dynamics may only possess stable isolated attractors, where portions of phase space are not sampled at all. However, when noise is added, mixing between the basins occurs. Therefore, in addition to having an invariant probability density from the noisy Frobenious–Perron formalism, we may also have a condition of noise-induced ergodicity based on noised induced transport. We have shown that stochastic flux is high precisely where necessary to complete the heteroclinic tangle. The tools we have used here may indeed be further pushed to possibly define a version of noise-induced chaos on a rigorous footing.

It is an amazing result that such transport between basins in random dynamical systems can be achieved without the manifold structure in hand. Our result not only reveals transport for a given model, it may be considered as a toolbox in which transport in random dynamical systems theory may be further developed, as in the rigorous style of [28].

Acknowledgements

EB is supported by the National Science Foundation under grant DMS-0071314. IBS is supported by the Office of Naval Research. LB is supported by the Office of Naval Research under grant N00173-01-1-G911.

Appendix A. Remarks on coarse-grids and Markov partitions

The goal of this section is to show that as the partition of rectangles $\{B_i\}$ is refined, the calculations based on a Galerkin's method approximation of the Frobenius–Perron operator improves. Luckily, our problem does not suffer many of the difficulties and questions of partitions inherent in the classic Ulam's conjecture.

The main difficulty in the Ulam's method literature is the question of whether the long term distribution resulting from repeated application of the matrix representation is adequate to weakly approximate the long-term distribution of the original dynamical system. It took from 1960 when Ulam stated the problem [19] until 1976 when Li [18] presented a first mathematical proof to rigorously solve Ulam's original problem for a special class of one-dimensional transformations. Indeed, there are technical requirements on the transformation, and the proof is not simple; there has been a great deal of work since Li to formulate similar statements for related problems in higher dimensions, or with other constraints on the transformation [29–34]. The main source of concern in such approximations is that the error in approximation may be propagated upon repeated application of the operators, as is necessary when considering the long-term steady-state solution. Fortunately, we are not concerned here with most of these referred to technical issues, since we investigate only the one-step action of the map on densities.

Now we justify the "$\simeq$" symbol, often used in previous sections to denote that the grid representation is a "good" approximation. First we show that one application of the stochastic Frobenius–Perron operator yields a continuous density function. This is not a surprising result, since the Frobenius–Perron operator is somewhat similar to a convolution of the initial density to the noise density. There is a similar result for normal noise, by Zeeman [35], but we include our proof here since it is specialized to our problem.

Theorem. *Suppose that the noise distribution $\nu \in C_0^0(M)$,[5] of the stochastic Frobenius–Perron operator, Eq. (7) is uniformly continuous, and given a continuous initial density function of compact support, $\rho_0(x) \in C_0^0(M)$, then the output density $\rho_1(x) = \int_M \nu(x - T(y))\rho_0(y)\,\mathrm{d}y$ is continuous on its domain, M.*

Proof. Since ν is continuous, by definition, there is $\delta(\bar{\epsilon})$ so that $|\nu(x + \delta(\bar{\epsilon})) - \nu(x)| < \bar{\epsilon}$, for all $\bar{\epsilon} > 0$, for all $x \in M$ by the assumption of uniformity. Therefore, we bound

$$\begin{aligned} |\rho_1(x + \delta(\bar{\epsilon})) - \rho_1(x)| &= \int_M |\nu(x + \delta(\bar{\epsilon}) - T(y)) - \nu(x - T(y))\rho_0(y)\,\mathrm{d}y| \\ &\leq \int_M |\nu(x + \delta(\bar{\epsilon}) - T(y)) - \nu(x - T(y))||\rho_0(y)|\,\mathrm{d}y \\ &< \int_M \bar{\epsilon}|\rho_0(y)|\,\mathrm{d}y \leq \bar{\epsilon}RT \leq \epsilon. \end{aligned} \tag{A.1}$$

The second inequality follows the uniform continuity of ν. The third inequality follows the assumption that $\rho_0(x) \in C_0^0(M)$, continuous functions of compact support, since the choice $R = \max_M \rho_0(x)$ exists and T is the Lebesgue measure of the compact region over which $\rho_0(x)$ is nontrivially supported. Finally, the fourth inequality follows since we have control in choosing $\bar{\epsilon}$ as small as needed to meet any initial choice of $\epsilon > 0$. □

Remark. In particular, the "$\simeq$" used throughout this paper relies first on Eq. (11), which for the choice of characteristic basis functions, refers to the statement that piecewise constant functions are dense in the continuous functions, $C_0^0(M)$.

Remark. The Frobenius-Perron operator, Eq. (7) is a bounded linear operator, as are its restricted-domain sub-operators, Eq. (23), which are also continuous operators [27]. Hence, any sequence of initial densities, $\rho_{0,N}$ (based on a fine grid of boxes $\{B_i\}_{i=1}^N$ of N-boxes) converging to $\rho_0 \in C_0^0(M)$ will yield output density functions $\rho_{1,N}$, which are likewise sup-norm close to ρ_1. Hence, the measures of transport in this paper, based on a fine grid covering of the phase space can be estimated and controlled.

[5] And continuous functions of compact support are dense in $L^p(M)$ for $p \geq 1$, [27].

Remark. A detail skipped by the previous remark is the fact that the diffusion [22] due to noise will cause $\rho_1(x)$ to have nonzero support on all of $\Re^n$, and hence not be of compact support. However, $\rho_1(x)$ is well approximated by continuous functions of compact support, and the above statement can be made rigorous for m-finite iterations. More work would be necessary in the limit $m \to \infty$, but the toolbox proposed here to study transport does not rely on this limit. We have discussed the one-step action of the map on densities. The exception to this statement is the expectation question studied in Section 9.

References

[1] J. García-Ojalvo, J.M. Sancho, Noise in Spatially Extended Systems, Springer, New York, 1999.
[2] L. Gammaitoni, P. Hanggi, P. Jung, F. Marchesoni, Stochastic resonance, Rev. Mod. Phys. 70 (1998) 223.
[3] S. Kadar, J. Wang, K. Showalter, Noise supported traveling waves in sub-excitable media, Nature 391 (1998) 770–774.
[4] M. Franaszk, E. Simiu, Auditory nerve fiber modeling: a stochastic Melnikov approach, Phys. Rev. E 57 (5) (1998) 5870–5876.
[5] S. Wiggins, Chaotic Transport in Dynamical Systems, Springer, New York, 1992.
[6] T.J. Kaper, S. Wiggins, An analytical study of transport in stokes flows exhibiting large-scale chaos in eccentric journal bearing, J. Fluid Mech. 253 (1993) 211–243.
[7] E. Simiu, Melnikov process for stochastically perturbed, slowly varying oscillators: application to a model of wind-driven coastal currents, J. Appl. Mech., Trans. ASME 63 (1996) 429–435.
[8] I. Schwartz, H. Smith, Infinite subharmonic bifurcations in an SEIR epidemic model, J. Math. Biol. 18 (1983) 233–253.
[9] T. Carr, L. Billings, I. Schwartz, I. Triandaf, Bi-instability and the global role of unstable resonant orbits in a driven laser, Physica D 147 (2000) 59–82.
[10] L. Billings, I. Schwartz, Exciting chaos with noise: unexpected dynamics in epidemic outbreaks, J. Math. Biol. 44 (2002) 31–48.
[11] G. Froyland, K. Aihara, Ulam formulae for random and forced systems, in: Proceedings of the 1998 International Symposium on Nonlinear Theory and its Applications, vol. 2, Crans-Montana, Switzerland, 1998, pp. 623–626.
[12] G. Froyland, K. Aihara, Estimating statistics of neuronal dynamics via Markov chains, Biol. Cyber., in press.
[13] I. Schwartz, Multiple stable recurrent outbreaks an predictability in seasonally forced nonlinear epidemic models, J. Math. Biol. 21 (1985) 347–361.
[14] I. Schwartz, Small outbreaks in seasonally driven epidemics, J. Math. Biol. 30 (1992) 473–491.
[15] D. Earn, P. Rohani, B. Bolker, B. Grenfell, A simple model for complex dynamical transitions in epidemics, Science 287 (2000) 667–670.
[16] A. Lasota, M.C. Mackey, Chaos, fractals, and noise, Stochastic Aspects of Dynamics, 2nd ed., Springer, New York, 1994.
[17] R. Courant, D. Hilbert, Methods of Mathematical Physics, vol. 1, Wiley, New York, 1970.
[18] T.Y. Li, Finite approximation for the Frobenius–Perron operator. A solution to Ulam's conjecture, J. Approx. Theory 17 (2) (1976) 177–186.
[19] S.M. Ulam, Problems in Modern Mathematics, Science Editions, Wiley, New York, 1964.
[20] R. Gould, Graph Theory, The Benjamin/Cummings Publishing Co. Inc., Menlo Park, CA, 1988.
[21] J.A. Bondy, U.S.R. Murty, Graph Theory with Applications, American Elsevier Publishing Co., Inc., New York, 1976.
[22] N.G. van Kampen, Stochastic Processes in Physics and Chemistry, Lecture Notes in Mathematics, North-Holland, Amsterdam, 1981, p. 888.
[23] W.H. Press, B.P. Flannery, S.A. Teukolsky, W.T. Vetterling, The art of scientific computing, Numerical recipes in C, Cambridge University Press, Cambridge, 1988.
[24] A. Ostruszka, P. Pakoński, W. Słomczyński, K. Życzkowski, Dynamical entropy for systems with stochastic perturbation, Phys. Rev. E 62 (2, Part A) (2000) 2018–2029.
[25] E. Bollt, Controlling chaos, targeting, and transport, Ph.D. Thesis, U. Colorado, Boulder, 1995.
[26] G. Golub, C.V. Loan, The art of scientific computing, Matrix Computations, 2nd ed., Johns Hopkins University Press, Baltimore, MD, 1989.
[27] N. Boccara, Functional Analysis: An Introduction for Physicists, Academic Press, San Diego, 1990.
[28] L. Arnold, Random Dynamical Systems, Springer, New York, 1998.
[29] A. Boyarsky, G. Haddad, All invariant densities of piecewise linear Markov maps are piecewise constant, Adv. Appl. Math. 2 (3) (1981) 284–289.
[30] G. Froyland, Finite approximation of Sinai–Bowen–Ruelle measures for Anosov systems in two dimensions, Random Comput. Dynam. 3 (4) (1995) 251–263.
[31] G. Froyland, Approximating physical invariant measures of mixing dynamical systems in higher dimensions, Nonlinear Anal. 32 (7) (1998) 831–860.
[32] A. Boyarsky, Y.-S. Lou, Approximating measures invariant under higher-dimensional chaotic transformations, J. Approx. Theory 65 (2) (1991) 231–244.
[33] J. Ding, A.H. Zhou, Piecewise linear Markov approximations of Frobenius–Perron operators associated with multi-dimensional transformations, Nonlinear Anal. 25 (4) (1995) 399–408.
[34] J. Ding, A.H. Zhou, The projection method for computing multidimensional absolutely continuous invariant measures, J. Statist. Phys. 77 (3–4) (1994) 899–908.
[35] E. Zeeman, Stability of dynamical systems, Nonlinearity 1 (1988) 115–155.